Journal of Materials Chemistry A

ROYAL SOCIETY OF CHEMISTRY

PAPER

View Article Online
View Journal

Cite this: DOI: 10.1039/d5ta04308e

Viscoelasticity-controllable dynamic borate polydimethylsiloxane networks for enhancing energy dissipation of elastomers†

Fu-Long Gong,[ab] Shuang Long,[ab] Wenqing Lv,[ab] Xiaotong Shu,[ab] Bin Huang,[a] Pingping Lou,[a] Hua-Feng Fei *[ab] and Zhijie Zhang[a]

Received 28th May 2025
Accepted 22nd July 2025

DOI: 10.1039/d5ta04308e

rsc.li/materials-a

Borosiloxane-based materials, such as polyborosiloxane (PBS) are ideally utilized as impact-protective materials due to their shear-stiffening behavior, providing effective protection against injury. Current strategies rely on blending them with functional fillers or scaffolds to enhance impact-protective performance or achieve specific functionalities. However, the unclear structure–property relationships of borosiloxane-based materials have hindered their further development. Herein, we utilize viscoelasticity-controllable dynamic borate PDMS networks (PPDBS) for constructing PPDBS/PDMS double-network elastomers (SSEs) that exhibit excellent energy dissipation properties. The ultrahigh energy dissipation characteristics of SSEs are attributed to the rapid characteristic relaxation and high internal friction inherent to the network. We found that SSEs not only exhibit excellent damping properties ($\tan\delta > 0.3$) over a broad frequency (0.01–50 Hz) and temperature (−20–140 °C) range, but also demonstrate superior impact-protective performance compared with most commercial materials, including PBS. This work opens up a new avenue for the design of high-performance impact-protective and damping materials.

1. Introduction

Impact-protective materials play a crucial role in attenuating the impacts of shock and vibration on industrial equipment, precision instrumentation, and human beings.[1–3] Smart materials hold significant potential for the design of next-generation impact-protective materials, as they can respond to external stimuli and undergo transition from a soft to a rigid state upon impact, thereby providing effective protection against injury.[4–8]

Borosiloxane-based materials, such as Silly Putty, also known as polyborosiloxane (PBS) or shear-stiffening gel (SSG), are typical smart materials that exhibit softness-stiffness switchability characteristics.[9–12] The fascinating viscoelasticity of these borosiloxane-based materials arises from the dynamic B–O bond exchange progress and the overall timescale of network rearrangement.[13–15] Specifically, these materials exhibit viscosity characteristics with flowability over long timescales and a rigid mechanical behavior at high strain rate. The combination of the dynamic B–O bond and the high mobility of polydimethylsiloxane units endows borosiloxane-based materials with unique properties, positioning them as a promising material for applications in shock-wave dissipation,[16] impact resistance,[17–20] flexible sensing,[21–25] battery protection,[26–28] mouthguards,[29] magnetorheological materials,[30] and other areas of contemporary significance. Inspired by the shear-stiffening behavior during the external impact, a series of products based on borosiloxane-based materials have also been fabricated and considered as a perfect fit for impact-resistant devices.[31,32]

Despite extensive exploration of blending polymer fluids,[33] various functional fillers or scaffolds with them to enhance performance or achieve specific functionalities, the fundamental understanding of structure–property relationships remains limited.[34] The architecture of the polymer plays a crucial role in determining the overall properties of dynamic networks.[35–37] Structural regulation of crosslinkers and topology optimization of borosiloxane-based materials are considered effective strategies to further enhance their impact-protective performance.[38,39] However, the unclear correlation between initial compositional parameters of borosiloxane-based materials and the resulting viscoelastic properties has hindered the optimization of energy dissipation characteristics and shear-stiffening behavior. This knowledge gap ultimately restricts the systematic enhancement of the impact-protective performance in borosiloxane-based materials, presenting a significant challenge for their advanced applications in impact protection.[40] Thus, this current work is aimed at providing a comprehensive understanding of the structure–property relationship of

[a]Key Laboratory of Science and Technology on High-tech Polymer Materials, Institute of Chemistry, Chinese Academy of Sciences, Beijing, 100190, P. R. China. E-mail: feihuafeng@iccas.ac.cn

[b]School of Chemical Sciences, University of Chinese Academy of Sciences, Beijing, 100049, P. R. China

† Electronic supplementary information (ESI) available. See DOI: https://doi.org/10.1039/d5ta04308e

borosiloxane-based materials for optimization of the performance of impact-protective materials.

In this study, we present a PPDBS/PDMS double-network elastomer (SSE) that exhibits remarkable energy dissipation characteristics and shear-stiffening behavior. These characteristics are achieved through the controlled regulation of the viscoelastic properties of borosiloxane-based materials (Fig. 1a). The PPDBS/PDMS double-network elastomer comprises two interpenetrating networks: a permanently crosslinked PDMS network and a dynamic borate PDMS network (PPDBS). The covalently crosslinked PDMS network provides structural stability and mechanical strength, while the fascinating viscoelastic properties of PPDBS contribute to the material's energy dissipation characteristics and shear-stiffening behavior (Fig. 1b). Because of the clarified structure–property relationship of PPDBS, precise enhancement of the elastomer's energy dissipation can be achieved through systematic regulation of the PPDBS network structure. Owing to the rapid characteristic relaxation and high internal friction inherent in elastomers, the prepared SSE-0.85-110k materials exhibit controllable high damping properties (tan δ > 0.3) across a broad frequency and temperature spectrum, along with significant impact-protective properties (Fig. 1c). We hope the present work can promote the development of high-performance impact-protective materials.

2. Results and discussion

2.1. Design principle of the PPDBS/PDMS double network elastomers and preparation of PPDBS networks

In this study, we conducted a one-pot procedure to prepare the PPDBS/PDMS double network elastomers as illustrated in Fig. 1b. PPDBS and the Pt catalyst (0.1 wt%) was added into the PDMS precursors and were mixed together, and then the mixture was poured into the model and cured at 120 °C for 2 h to obtain PPDBS/PDMS double-network elastomers. The structural architecture of the elastomers features a dual-network system consisting of two interpenetrating polymeric networks: (1) a permanently crosslinked polydimethylsiloxane (PDMS) network and (2) a dynamic borate PDMS network (PPDBS). We used the condensation reaction between 1,4-phenylenediboronic acid (PDBA) and siloxane diols (PDMS-OH) to form the PPDBS networks. Concurrently, covalently crosslinked PDMS networks were engineered through platinum-catalyzed Si–H/C=C coupling to establish permanent network connectivity. These distinct reactions facilitated the formation of a dual-network system comprising two interpenetrating polymeric networks.

The dynamic borate PDMS network (PPDBS) was initially investigated to understand the relationship between the

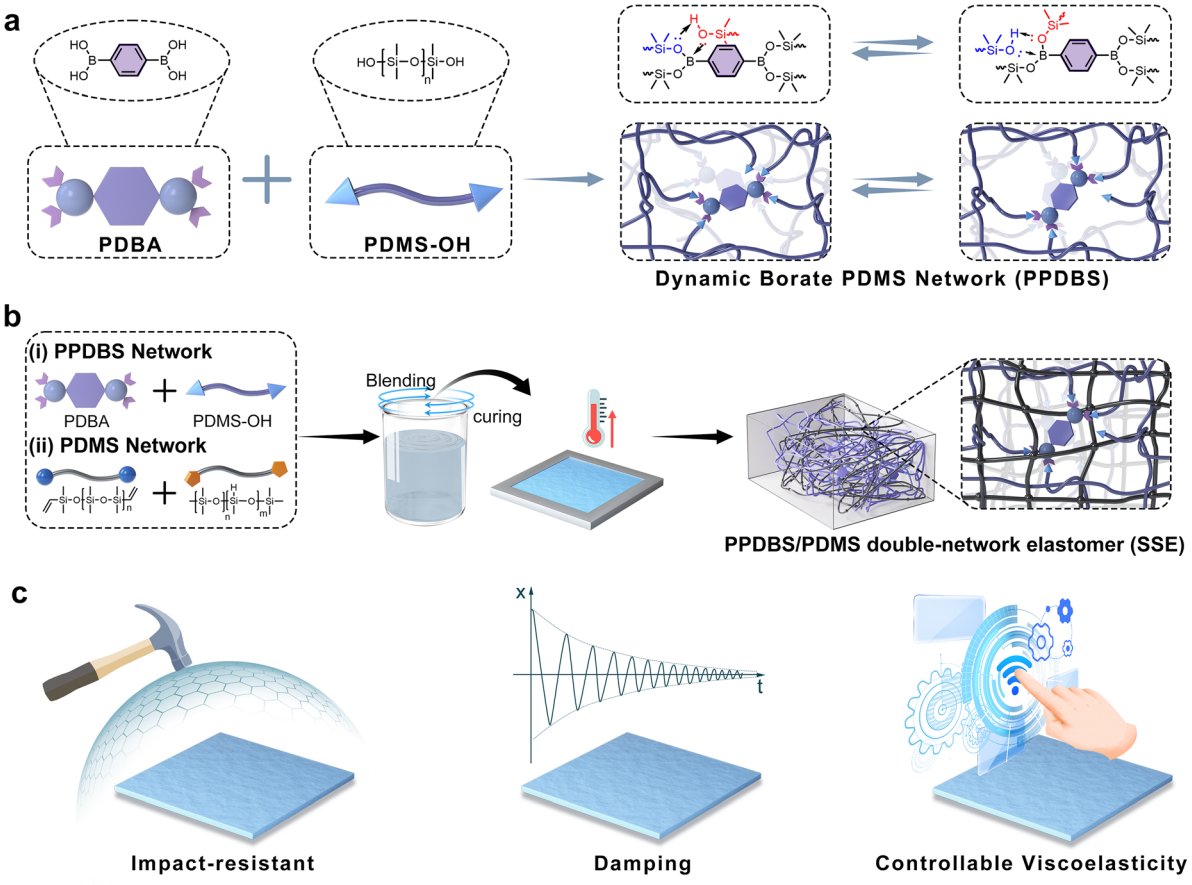

Fig. 1 Schematic illustration of the preparation procedure and characteristic of the PPDBS/PDMS double network elastomers. (a) Preparation of the dynamic borate PDMS network (PPDBS) and the dynamic exchange progress of the B–O bond. (b) Preparation of the PPDBS/PDMS double network elastomer. (c) Characteristics of the PPDBS/PDMS double network elastomers.

viscoelastic properties and the initial materials. The condensation reaction between 1,4-phenylenediboronic acid (PDBA) and siloxane diols (PDMS-OH) with varying molecular weights was employed to form the PPDBS networks (Tables S1 and S2†). Representative images of these materials are shown in Fig. S1† and 2a. For convenience, the resulting materials are denoted as PPDBS*x*, where *x* indicates the molecular weight of the PDMS-OH.

To systematically investigate the influence of cross-linker structure on the viscoelastic properties of the dynamic borate PDMS network, PBS networks were also synthesized for comparative analysis (Fig. S2†). The molecular structures of PPDBS networks were characterized using ATR-FTIR and solid-state ^{11}B MAS NMR spectroscopy. The FT-IR spectra revealed the absence of signals above 3000 cm^{-1} and the presence of a Si–O–B bond at 1340 cm^{-1}, indicating the formation of Si–O–B bonds through mutual condensation of B–OH and Si–OH groups (Fig. 2b).[38] No tetragonal B–O asymmetric stretching bands (1050–850 cm^{-1}) were observed in the FT-IR spectra, confirming that boron atoms are covalently bonded to silicone backbones in PPDBS.[16] The new peaks at 1310 cm^{-1} and 1290 cm^{-1} correspond to organic vibrations of the phenyl ring. Additionally, the intensity of the Si–O–B bond at 1340 cm^{-1} gradually decreased from PPDBS1200 to PPDBS110000 due to decreasing boron content (Fig. 2c).

To further probe the chemical environment of the boron centers on PPDBS networks, ^{11}B MAS NMR was conducted on PDBA, PPDBS1200, PPDBS4200, and PBS1200 (Fig. 2d). The aromatic ring in PPDBS1200 resulted in a higher chemical shift compared to PBS1200, and the broad chemical shift was attributed to the local disorder present in PPDBS networks.[14] In addition, a single broad peak around 22 ppm was consistent with a trigonal boron species that decreased with the decreasing boron contents, which ruled out the possibility of any dative bonding in the PPDBS networks.[41] The glass transition temperature (T_g) of the dynamic networks was measured using differential scanning calorimetry, and for both PPDBS and PBS, a rise in T_g was noted when the crosslink density rose (Fig. S5†). Furthermore, PPDBS networks demonstrated superior thermostability, thereby broadening their application temperature range (Fig. S7†).

2.2. Viscoelasticity investigation of dynamic borate PDMS networks

To investigate the impact of network structure on the viscoelastic properties of PPDBS networks, oscillatory shear

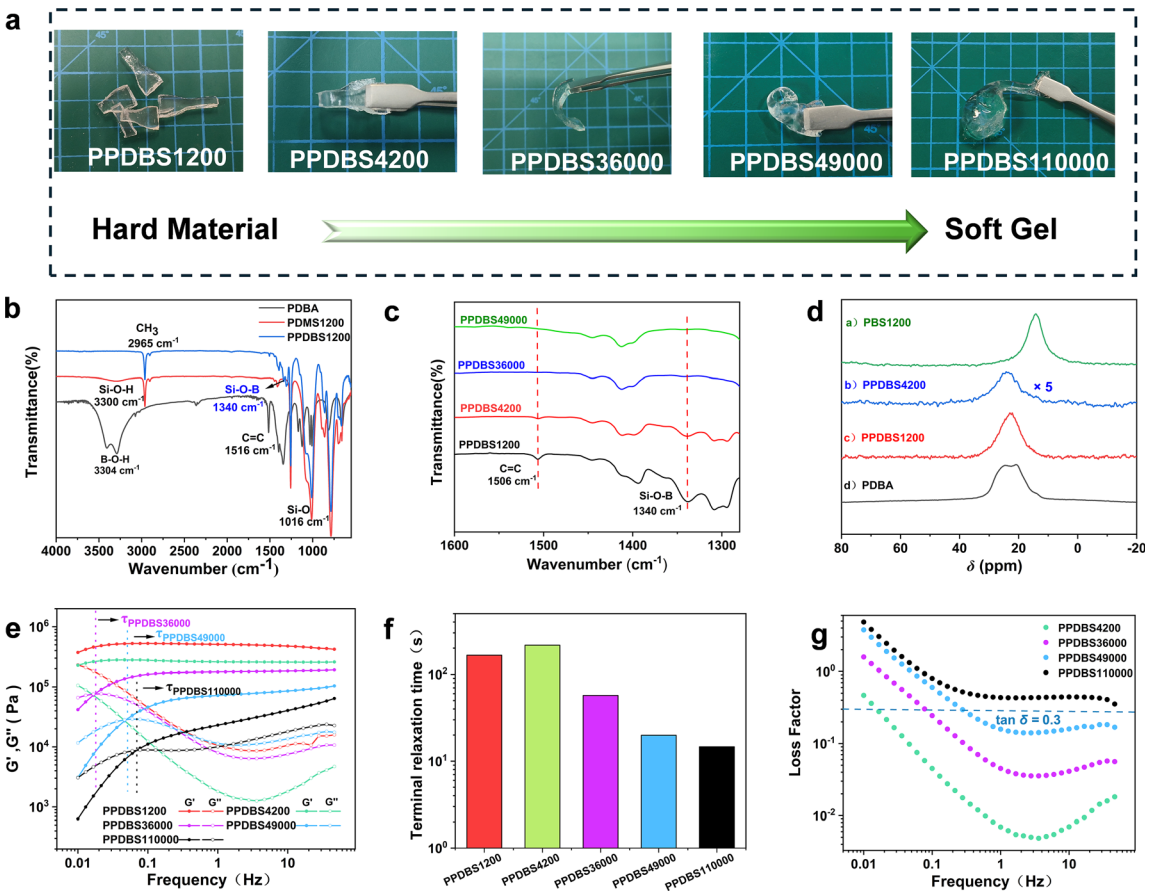

Fig. 2 Characterization and viscoelastic properties of PPDBS networks. (a) Photographs of the PPDBS networks. All the samples are optically transparent. (b) FT-IR spectra of PDBA, PDMS1200, and PPDBS1200. (c) FT-IR spectra of PPDBS networks with varied crosslinking densities. (d) ^{11}B MAS NMR of PBS1200, PPDBS4200, PPDBS1200, and PDBA. (e) Frequency dependence of the storage modulus (G') and loss modulus (G'') for PPDBS networks. The τ_c values of PPDBS networks are labelled by dashed lines and arrows. (f) The terminal relaxation times of PPDBS networks. (g) Frequency dependence of the loss factor (tan δ) for PPDBS networks.

rheological frequency sweeps were conducted over a range of 0.01 to 50 Hz for these materials. As shown in Fig. 2e, all samples exhibited characteristic viscoelastic behavior, maintaining a rubbery plateau at higher frequencies with storage moduli (G') ranging from 50 kPa to 500 kPa, which increased with the increasing crosslink density. Below the crossover frequency (where $G' = G''$), the networks displayed fluid-like behavior analogous to PBS, as evidenced in Fig. S9.†[42] Notably, PPDBS1200 and PPDBS4200 exhibited no crossover within the measured frequency range, suggesting that their transition frequency occurs below 0.01 Hz. To further comprehensively understand the viscoelastic properties of the PPDBS networks, we plotted master curves following the time–temperature superposition (TTS) at the reference temperature of 25 °C (Fig. S11–S14†). The activation energy (E_a) was obtained from the horizontal shift factors (a_T) as a function of temperature, and a decrease in E_a with decreasing crosslink density was observed (Fig. S11–S14†) which is consistent with other telechelic networks.[43]

The characteristic relaxation time (τ_c), defined as the reciprocal of the crossover frequency, was measured at 167 s, 216 s, 57 s, 20 s, and 14 s for PPDBS1200, PPDBS4200, PPDBS36000, PPDBS49000, and PPDBS110000, respectively (Fig. 2f). The crossover was denied where $G' = G''$ corresponding to the transition from a viscoelastic solid to a viscoelastic liquid. Thus, the increase in τ_c indicated that PPDBS networks exhibit more solid-like behavior with increasing crosslink density, and high dynamic crosslink density can inhibit flow, which is similar to PBS (Fig. S9†).[13,16] Additionally, PPDBS4200 samples with 90%, 75%, and 60% Si–OH group reacted with PDBA were synthesized to verify the relationship between the characteristic relaxation time and free OH groups. With an increasing number of free Si–OH groups present, the characteristic relaxation time decreased significantly from 216 s down to just 11 s due to the faster exchange rate of the Si–O–B dynamic bond (Fig. S10†). Therefore, the shorter τ_c for PPDBS1200 compared to PPDBS4200 was primarily attributed to the residual OH groups. We investigated the impact of crosslink density on the loss factor of PPDBS, as loss factor is a critical parameter for characterizing the energy-dissipation properties of materials (Fig. 2g). The loss factor of PPDBS increased within the frequency range of 0.01 Hz to 50 Hz as the crosslink density decreases. Notably, PPDBS110000 demonstrated superior damping performance ($\tan\delta > 0.3$) over a wide frequency range due to the rapid characteristic relaxation and high internal friction inherent to the network.[44] To further investigate the characteristic relaxation behavior of PPDBS resulting from the dynamic covalent Si–O–B bonds, temperature-sweep rheological tests were conducted on PPDBSx at a frequency of 1 Hz (Fig. S16a†).

Below the crossover temperature ($T_{crossover}$), where storage modulus (G') equals loss modulus (G''), all PPDBS samples exhibited rubbery behavior, with the storage modulus increasing monotonically as crosslink density increased. Above $T_{crossover}$, flow behavior was observed in the materials. An increasing plateau modulus as a function of temperature was observed, providing evidence that the network topology remains conserved.[13,43] Furthermore, the high damping performance of PPDBS110000 was also observed in temperature sweep rheological curves, with the loss factor consistently exceeding 0.4 across the entire test temperature range (Fig. S16b†). These results highlight the critical role of molecular weight optimization in tailoring the viscoelastic properties of the PPDBS networks.

2.3. Design of high damping PPDBS networks over a wide frequency spectrum

Through the investigation of PPDBSx materials, two siloxane diols (PDMS-OH) with different chain lengths were condensed with PDBA to form the PPDBS-y (y denotes the M_w of high molecular weight PDMS-OH). While the low molecular weight PDMS-OH provides stiffness, the high molecular weight PDMS-OH enhances the material's capacity for rapid characteristic relaxation. By varying the chain length of the high molecular weight PDMS-OH (Table S2†), we examined the molecular dependence of shear stiffening behavior and energy dissipation properties in PPDBS-y (Fig. 3a). The relative shear-stiffening effect (RSTe) was chosen to characterize the shear stiffening behavior,[45] and determined as follows:

$$\mathrm{RSTe} = \frac{G'_{50\ \mathrm{Hz}} - G'_{0.01\ \mathrm{Hz}}}{G'_{0.01\ \mathrm{Hz}}}$$

As shown in Fig. 3b and c, both the loss factor ($\tan\delta$) and RSTe values exhibited a monotonic increase with increasing molecular weight of PDMS-OH, demonstrating a strong molecular weight–property correlation. This systematic approach led to the development of PPDBS-110k, which demonstrated optimal performance characteristics, including exceptional damping properties ($\tan\delta > 0.5$) across a broad frequency range and superior shear stiffening behavior (RSTe = 100). In contrast, PDMS exhibited significantly lower damping properties, with a loss factor of less than 0.05 throughout the measured frequency spectrum (Fig. 3d). Furthermore, the impact resistance of the materials was quantitatively assessed through drop-ball impact testing.[46] In this experimental setup, a steel ball was released from a fixed height onto 2 mm thick samples, while force sensors recorded the impact dynamics in real-time. As illustrated in Fig. 3e, PPDBS-110k demonstrated exceptional shock wave attenuation capabilities. Comparative analysis indicated that PPDBS-110k significantly prolonged the cushioning times and reduced the maximum impact force (Fig. 3f), representing a substantial enhancement in impact resistance compared to other PPDBS and PDMS. The combination of exceptional damping performance ($\tan\delta > 0.5$), superior shear stiffening behavior (RSTe = 100), and enhanced impact resistance establishes PPDBS-110k as a promising material for advanced impact-protective applications.

2.4. Formation and mechanical properties of PPDBS/PDMS double-network elastomers (SSEs)

Based on the investigation of PPDBSx and PPDBS-y, we further examined the effects of embedding PPDBS into permanently

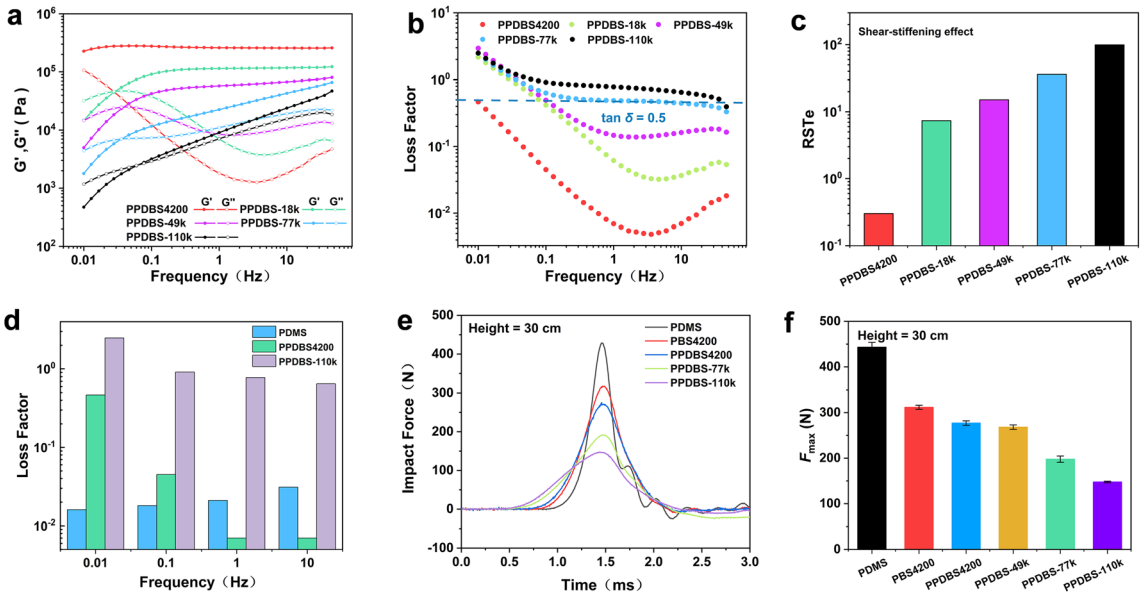

Fig. 3 Optimization of the energy-dissipation properties of the PPDBS networks. (a and b) Frequency dependence of storage modulus (G'), loss modulus (G''), and loss factor (tan δ) for PPDBS networks. (c) Relative shear-stiffening effect (RSTe) of PPDBS networks. (d) Loss factors of PDMS, PPDBS4200, and PPDBS-110k at different frequencies. (e) Force–time curves of PDMS, PBS4200 and PPDBS networks during the impact test when the ball dropped from a height of 30 cm. (f) Maximum impact force of PDMS, PBS4200 and PPDBS networks (error bars: SD, $n = 3$).

crosslinked PDMS networks. A series of PPDBS/PDMS double-network elastomers (SSEs) were synthesized by embedding different PPDBS-*y* contents into the PDMS networks. The resulting materials were named SSE-*x*-*y*, where *x* denotes the weight fraction of the PPDBS. Tables S3 and S4† detail the stoichiometric ratios of the raw materials used in the preparation of SSEs. Fig. S3† demonstrates the FT-IR spectra of dimethylhydrogen siloxane, PDMS, PPDBS-110k, and SSE-*x*-110k. The absence of signals at 2160 cm^{-1} and the presence of a Si–O–B bond at 1340 cm^{-1} indicate the successful formation of PDMS/PPDBS double-network elastomers.[47] We first conducted a macroscopic observation of these samples. As shown in Fig. 4a, PPDBS gradually underwent irreversible deformation. In contrast, SSEs maintained excellent shape stability throughout the observation period owing to the incorporation of a permanently crosslinked network. The optical properties were quantitatively evaluated *via* UV-vis transmission spectroscopy of 2-mm-thick films (Fig. 4b). The SSEs exhibited remarkable optical transparency, exceeding 93% across the visible spectrum, comparable to that of PDMS, which indicates uniform dispersion and interpenetration of the two networks. Furthermore, the uniform surface morphology observed through SEM, combined with the homogeneous elemental distribution demonstrated by EDS mapping, confirmed the excellent compatibility between the two networks (Fig. 4c).

To evaluate the influence of PPDBS content and network architecture on mechanical performance, tensile tests were conducted on these samples (Fig. 4d, S23 and 24†). As shown in Fig. 4d, the mechanical properties exhibited significant composition dependence: increasing the PDMS content from 15% to 50% (w/w) enhanced the mechanical strength from 0.11 ± 0.01 MPa to 1.28 ± 0.05 MPa, while concurrently improving the elastic modulus. Remarkably, all SSEs maintained exceptional elongation properties, with strain at break consistently exceeding 150%. Control experiments with constant PDMS content (50% w/w) but varying PPDBS network structure revealed comparable mechanical strength across different formulations, confirming that the permanent PDMS network primarily governs the mechanical strength of SSEs (Fig. 4e).[47,48] Furthermore, the strain-rate-dependent mechanical properties of PPDBS, PDMS and SSEs were investigated through tensile and compression stress–strain tests. As shown in Fig. S25,† slow stretching of the PPDBS resulted in low stress yield (34 kPa) and unrecoverable deformation, attributed to the time-dependent dissociation and reconfiguration of dynamic bonds within the PPDBS network. In contrast, at elevated strain rates (>100 mm min^{-1}), the insufficient time for the dynamic bonds to break and dissipate energy resulted in increased fracture stress and reduced elongation at break, characteristic of the shear-stiffening effect. Such a shear-stiffening effect could also be observed in SSEs. The elastic moduli and fracture stress of SSEs increased with increasing tensile rates as shown in Fig. 4f and S26.† In addition to tensile tests, compressive stress–strain experiments on SSEs also indicated rate-dependent mechanical properties (Fig. 4g and S27†). Specifically, under identical strain conditions, the compressive stress and elastic moduli of SSEs increased with higher strain rates, as illustrated in Fig. 4g. By contrast, the permanently crosslinked PDMS network exhibited no strain-rate-dependent mechanical properties in either tensile or compressive tests (Fig. S28†). These findings indicated that while the PDMS network governs the fundamental mechanical properties, the PPDBS confers shear-stiffening behavior without compromising structural integrity.

Based on the reversible equilibria of dynamic B–O bond, the incorporation of PPDBS can endow SSEs with abundant energy

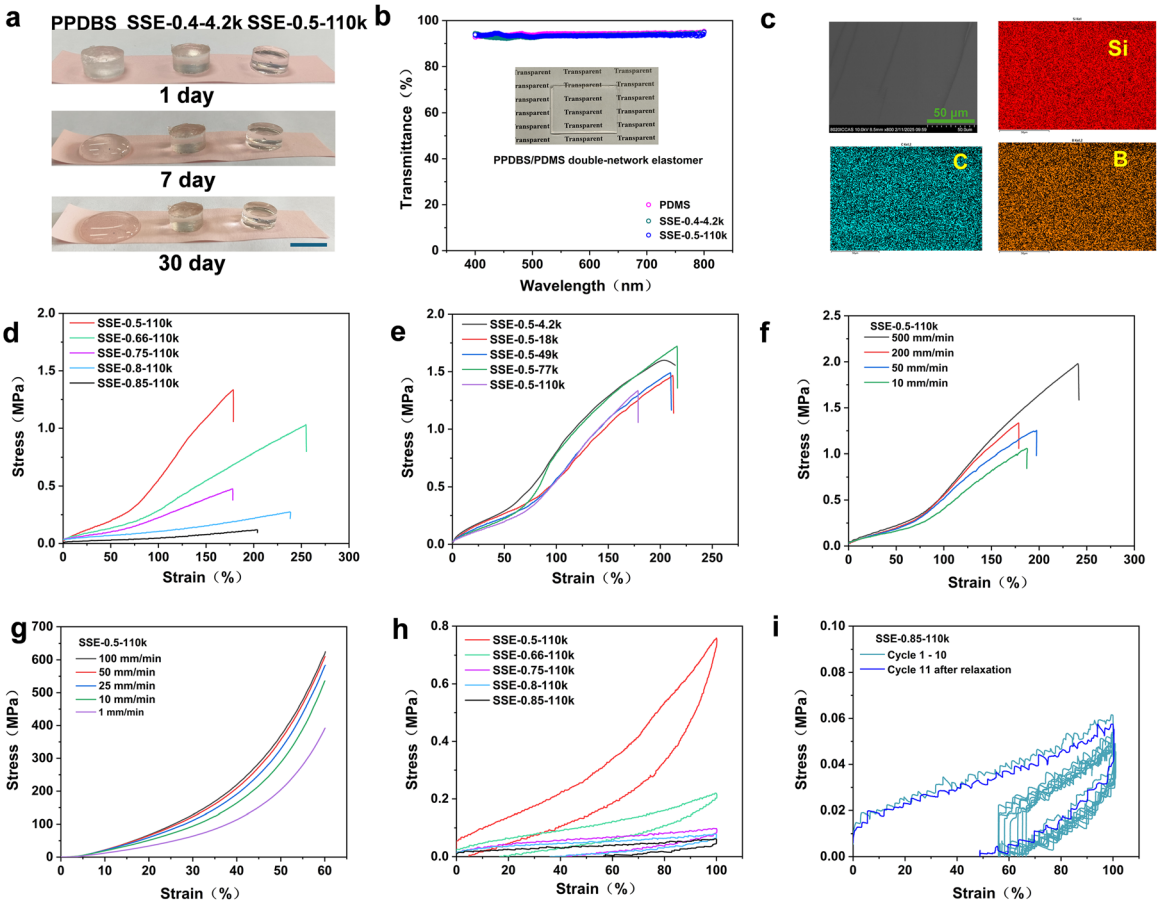

Fig. 4 Optical properties and mechanical properties of SSEs: (a) optical images of PPDBS4200 (left), SSE-0.4-4.2k (mid) and SSE-0.5-110k (right) at different times, scale bar: 1 cm. (b) UV-vis transmission spectroscopy of PDMS, SSE-0.4-4.2k and SSE-0.5-110k films. (c) Microscopic morphology of SSE-0.5-110k and element distribution determined using a scanning electron microscope, scale bar: 50 μm. (d) Tensile stress–strain curves of SSEs with varied contents of PPDBS-110k. (e) Tensile stress–strain curves of SSEs with varied contents of PPDBS networks. (f) Tensile stress–strain responses of SSE-0.5-110k at different tensile rates. (g) Compressive stress–strain responses of SSE-0.5-110k at different tensile rates. (h) Cyclic tensile tests of SSEs. (i) Ten consecutive cyclic tensile curves of SSE-0.85-110k at 100% strain; the second tensile started at 120 s intervals.

dissipation outlets during the impact. Consequently, we investigated the energy dissipation properties of SSEs *via* cyclic tensile tests. As illustrated in Fig. 4h, the loading and unloading curves of SSE-*x*-110k at a strain of 100% were analyzed, revealing that SSEs with higher PPDBS-110k content exhibited significant hysteresis loops and pronounced stress relaxation. The energy dissipation ratios of SSEs increased with increasing PPDBS-110k content. Specifically, the energy dissipation ratios for SSE-0.5-110k, SSE-0.66-110k, SSE-0.75-110k, SSE-0.8-110k, and SSE-0.85-110k were determined to be 39.0%, 46.6%, 66.4%, 66.8%, and 74.3%, respectively (Fig. S29†). These trends could be attributed to the introduction of PPDBS-110k, which improved the energy dissipation of the SSEs. Furthermore, cyclic stretching tests with increased strain were conducted on SSE-0.85-110k.[49] The results revealed that the hysteresis loop area gradually increased with increasing strain, suggesting enhanced energy dissipation at elevated strain levels. This phenomenon was mainly attributed to the dissociation and reconfiguration of dynamic B–O bonds within the material during stretching progress (Fig. S30†). To assess the elastic recovery behavior of the SSEs, the elastic recoverability of SSEs was validated by subsequent experiments: SSE-0.5-110k fully recovered to its original state within 20 seconds after undergoing a 200% strain deformation (Fig. S31†). Furthermore, cyclic tests over 10 cycles were conducted without any waiting time between consecutive tests, as shown in Fig. 4i and S32.† The energy dissipation in the second cycle was significantly lower than in the first cycle, likely due to insufficient time for the dynamic B–O bonds to fully return to their original state. After a 2-minute rest period following cyclic stretching, the 11th stretching cycle was performed on SSE-0.85-110k and displayed a curve nearly overlapped with the original, as illustrated in Fig. 4i. These findings demonstrated that SSEs exhibited excellent elastic recovery due to the incorporation of the permanent crosslinked PDMS network.

2.5. Viscoelasticity investigation of PPDBS/PDMS double-network elastomers (SSEs)

SSEs with constant PDMS content (50% w/w) but varying PPDBS network structures were first synthesized to verify the

composition dependence of damping properties and shear-stiffening behaviors. Fig. 5a presents the rheological master curves of SSE-0.5-*y*. Notably, SSE-0.5-110k exhibited a significantly sharper modulus response to frequency compared with other SSEs with the same PDMS content, attributable to the superior shear-stiffening behavior of PPDBS-110k. In contrast, for SSE-0.5-4.2k, the storage moduli were much larger than the loss moduli at higher frequencies, resulting in a relatively lower loss factor (Fig. 5c). It also suggested the critical role of the structure control of the PPDBS structure in tailoring the damping properties and shear-stiffening behaviors of the SSEs.

The dynamic viscoelastic properties of SSEs containing varied PPDBS contents were characterized through oscillatory frequency sweep measurements (0.1–50 Hz) at 25.0 °C. Fig. 5b shows the rheological master curves of SSEs with different PPDBS-110k contents. All SSEs demonstrated predominant elastic behavior with storage modulus (G') exceeding loss modulus (G'') throughout the tested frequency regime, confirming the structural integrity imparted by the permanently crosslinked PDMS network.[33] Furthermore, all SSEs exhibited an increase in storage moduli (G') as the frequency increased, confirming that the introduction of PPDBS-110k imparts shear-stiffening behavior to the SSEs. A more pronounced modulus response to frequency changes was observed, when the PPDBS content elevated from 50% to 85% (w/w). This trend was quantitatively supported by the relative shear-stiffening effect (RSTe) values of these samples. The RSTe values of the SSE-0.5-110k, SSE-0.66-110k, SSE-0.75-110k, SSE-0.8-110k and SSE-0.85-110k were 1.6, 3.0, 4.8, 6.5, and 9.5, respectively. A similar trend was also observed in SSEs containing varying PPDBS4200 contents (Fig. S19†). Subsequent analysis of energy dissipation properties was conducted through frequency-dependent loss

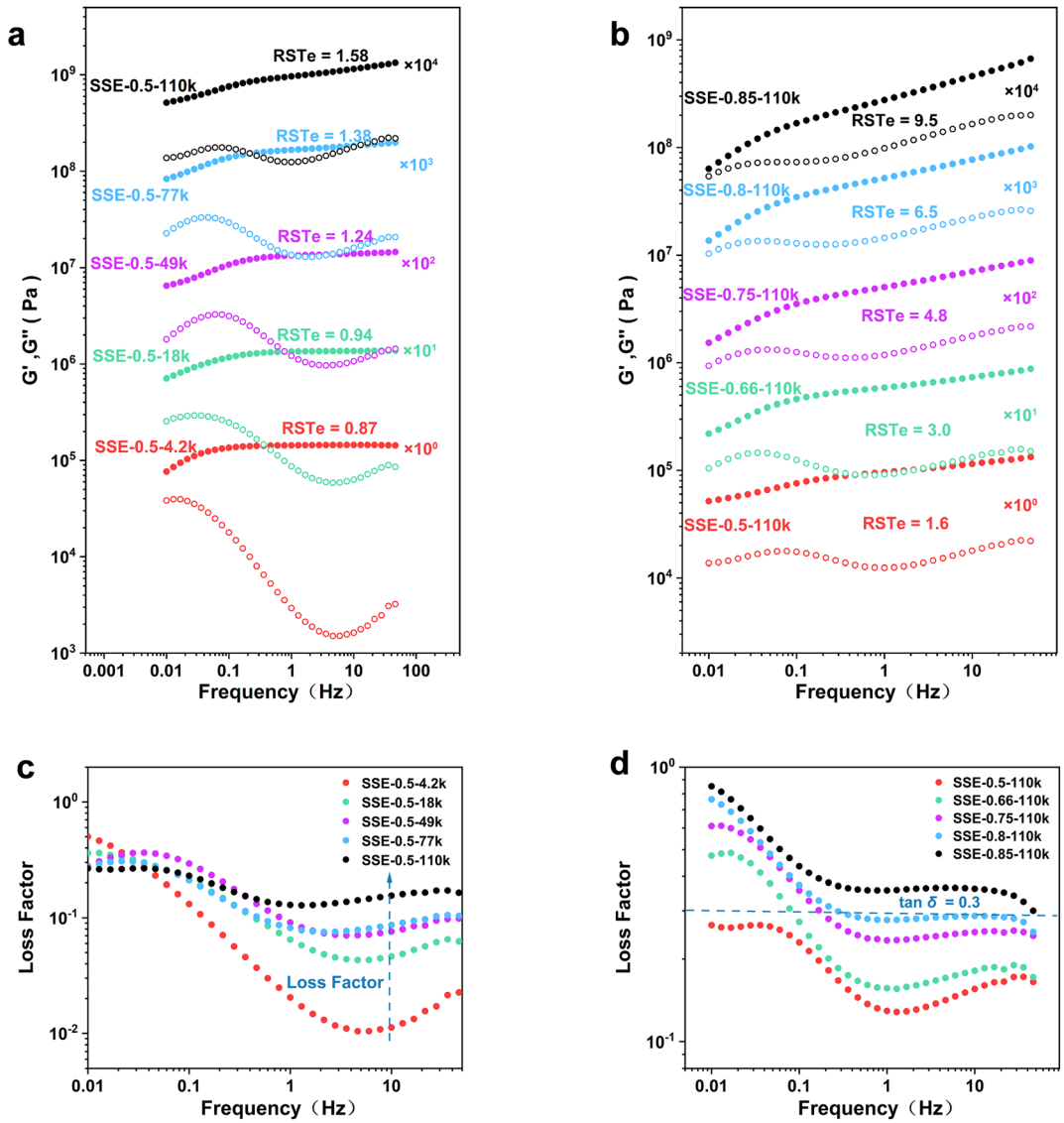

Fig. 5 Viscoelastic properties of SSEs with constant PDMS contents or varied PPDBS-110k contents. (a and c) Frequency dependence of storage modulus (G'), loss modulus (G''), and loss factor (tan δ) for SSEs with constant PDMS content. (b and d) Frequency dependence of storage modulus (G'), loss modulus (G''), and loss factor (tan δ) for SSEs with varied PPDBS-110k contents.

factor ($\tan\delta = G''/G'$) master curves (Fig. 5d). For SSE-*x*-110k, there was a wide damping peak near 0.01 Hz resulting from the characteristic relaxation of the dynamic crosslinked PDMS network (PPDBS). As the PPDBS-110k content increased from 50% to 85% (w/w), the loss factor of the SSEs consistently increased across the whole test frequency range. Remarkably, an elastomer (SSE-0.85-110k) exhibiting excellent damping properties ($\tan\delta > 0.3$) over a broad frequency range was successfully developed, which was attributed to the rapid characteristic relaxation and high internal friction inherent to the network (Fig. S21†).

These findings demonstrated that strategic tuning of the compositions of the SSEs enables precise control of energy dissipation, establishing a materials design paradigm for developing elastomers with excellent damping performance and shear-stiffening behavior. Furthermore, the high damping performance of SSE-0.85-110k was also assessed by temperature ramping tests (Fig. S22†). As illustrated in Fig. S21a,† both the storage modulus (G') and the loss modulus (G'') decreased insignificantly as the temperature increased from −20 to 140 °C, indicating the stability of the polymeric network. Notably, the loss factor of SSE-0.85-110k remained above 0.3 across the entire test temperature range, indicating its excellent damping performance over a wide temperature range. Consequently, through precise structural optimization, SSE-0.85-110k successfully integrated superior energy dissipation properties with excellent shear-stiffening behavior, outperforming both commercial silicone rubber and previously reported shear-stiffening elastomers (Fig. 6a).[29,38,50–52]

2.6. The energy dissipation properties of PPDBS/PDMS double-network elastomers (SSEs)

The excellent energy dissipation properties and shear stiffening behavior endowed SSE-0.85-110 with extraordinary shock

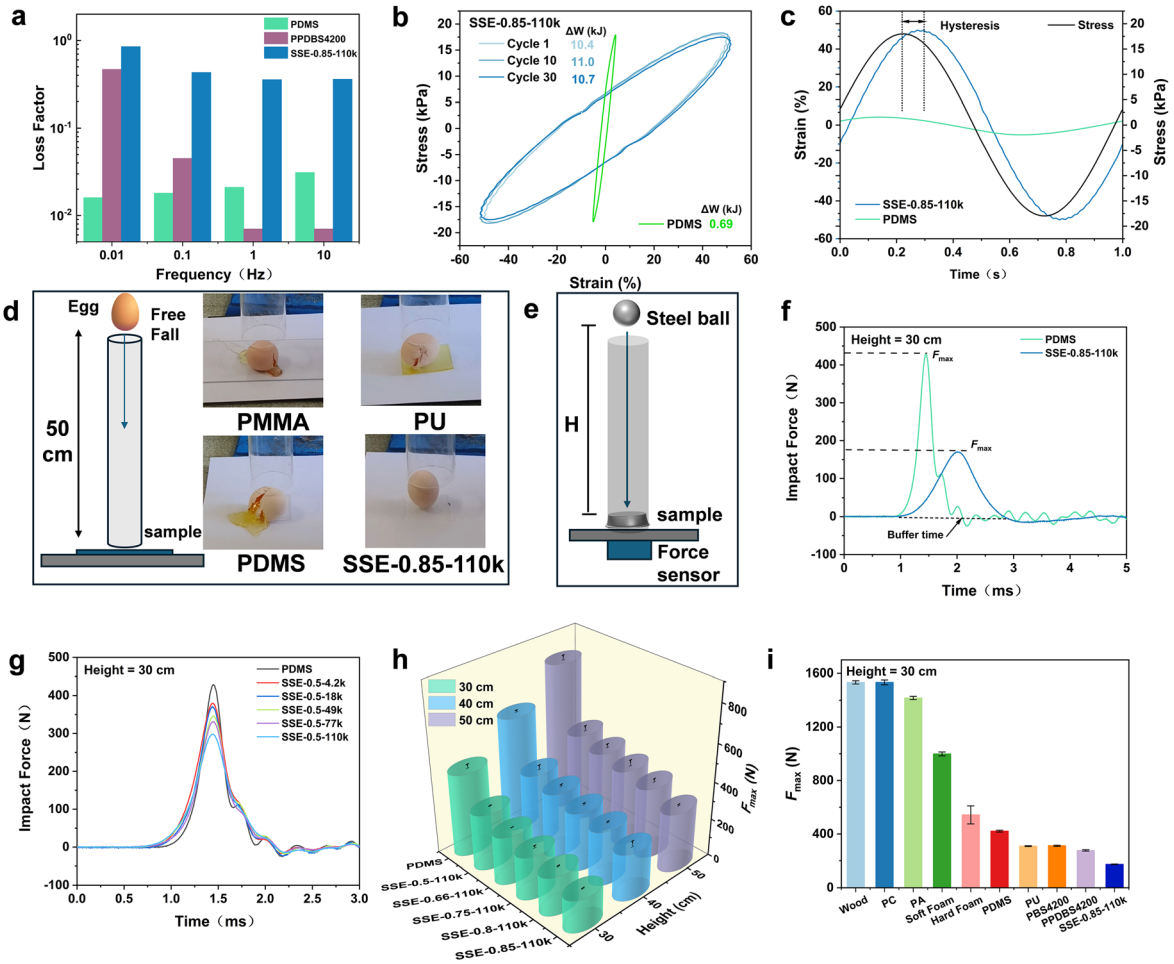

Fig. 6 The energy dissipation properties of SSEs. (a) Loss factors of PDMS, PPDBS4200, and SSE-0.85-110k at different frequencies. The loss factor of SSE-0.85-110k remained above 0.3 across the entire test frequency range. (b) Large amplitude oscillatory shear (LAOS) tests of PDMS and SSE-0.85-110k with 18 kPa stress. (c) The amplitude of the original vibration signal. (d) A raw egg dropped from 50.0 cm onto a 2.0 mm-thick protective material, only the egg dropped onto SSE-0.85-110k remained unbroken. (e) Schematic illustrating the equipment of the dropping ball impact experiment. (f) Force–time curves of PDMS and SSE-0.85-110k obtained from the dropping ball impact test. The F_{max} and buffer time are labeled by dashed lines and arrows. (g) Force–time curves of PDMS and SSE-0.5-*y* during the impact test when the ball dropped from a height of 30 cm. (h) Maximum impact force of PDMS and SSE-*x*-110k when impacted at different heights (error bars: SD, $n = 3$). (i) Maximum impact force of common materials, PBS, PPDBS and SSE-0.85-110k (error bars: SD, $n = 3$).

absorption and impact-protective performance. To further assess the shock absorption performance of SSE-0.85-110k, a periodic sinusoidal alternating stress of 18 kPa was applied to SSE-0.85-110k (Fig. 6b). The resulting stress–strain curves formed elliptical loops, referred to as hysteresis loops, indicating that SSE-0.85-110k remained within the linear viscoelastic region at strains up to 50%.[53,54] The energy dissipation in each cycle could be calculated by integrating the area of the hysteresis loop. Notably, the energy dissipation (ΔW) of SSE-0.85-110k was approximately 15.5 times greater than that of PDMS. Furthermore, the energy dissipation remained steady even after 30 cycles, confirming the excellent fatigue resistance of SSE-0.85-110k. As shown in Fig. 6c, significant hysteresis was observed in the stress–strain curves, which can be attributed to damping effects, indicating substantial internal friction inherent to the elastomers. To visually demonstrate the impact-protective performance of the material, a free-fall experiment was conducted by dropping a raw egg from a height of 50.0 cm onto a 2.0 mm-thick SSE-0.85-110k film (Video S1†). As shown in Fig. 6d, only the raw egg with the protection of the SSE-0.85-110k film remained intact, indicating a superior buffering effect compared with other materials. In order to have a further intuitive feeling of the energy dissipation properties, a rebound test was carried out as shown in Fig. S33.†[55] A steel ball (mass = 20 g) was released from a height of 20.0 cm onto both PDMS and SSE-0.85-110k substrates, while the start height (h) and the rebound peak height (r) was recorded to calculate the rebound ratio (defined as r/h). When the steel ball was dropped onto SSE-0.85-110k, the rebound ratio was only 0.125, significantly lower than that of PDMS (0.5), which suggests the high damping capability of SSE-0.85-110k.

To quantitatively evaluate the impact-protective performance of the SSEs, a drop ball impact experiment was conducted on various materials. When the steel ball freely dropped onto the force sensor covered with the protective material, part of the impact energy was absorbed by the material, while the residual force propagated through the material and was recorded by the force sensor (Fig. 6e).[56] Fig. 6f demonstrates the force time curves for PDMS and SSE-0.85-110k when the ball was dropped from the setting height.[57] For the group with PDMS as the buffer material, a high impact force of 443 ± 10 N and short buffer time of 1 ms were observed. By contrast, SSE-0.85-110k showed a lower peak force (173 ± 2.5 N) as well as longer buffer time (2 ms) than that of PDMS. Furthermore, the maximum force of SSE-0.85-110k was only 5.2% of that of the blank group, indicating that the mechanical impact damage was effectively suppressed. To establish comprehensive structure–property correlations, we systematically investigated the impact resistance of SSEs with fixed PDMS content (50% w/w) but varying PPDBS network architectures. Fig. 6g illustrates that SSE-0.5-110k could significantly reduce the maximum impact force compared with other samples, which was attributed to its high energy dissipation properties at high velocity impacts. It also suggested the role of structural control in tailoring the final properties of the SSEs. The impact-protective properties of SSEs containing varied PPDBS contents were also studied (Fig. S34†). As demonstrated in Fig. 6h, SSEs with higher contents of PPDBS-110k consistently exhibited lower maximum force across all heights, which is attributed to the enhanced energy dissipation properties conferred by PPDBS-110k. In addition, a comparative analysis of the impact performance of SSE-0.85-110k with common materials was conducted (Fig. S35†).[58] Among all the materials tested, SSE-0.85-110k exhibited a significantly faster attenuation of the generated impact, showcasing superior impact-protective performance compared to all control materials, including PBS and PPDBS (Fig. 6i).

3. Conclusion

In summary, we have developed a novel strategy in which the viscoelastic properties of dynamic borate PDMS networks were regulated for optimization of the energy dissipation and impact-protective performance of PPDBS/PDMS double-network elastomers. Given that the structure–property relationships of the dynamic borate PDMS network were comprehensively understood by rheological analysis, we can precisely enhance the energy dissipation properties and shear-stiffening behavior of the elastomers by modifying either the network structure or its content. It is found that SSE-0.85-110k exhibits excellent damping properties ($\tan\delta > 0.3$) over a broad frequency and temperature range, outperforming both commercial silicone rubber and previously reported shear-stiffening elastomers. More importantly, SSE-0.85-110k demonstrated a significantly faster attenuation of the generated impact, showcasing excellent impact-protective performance. Therefore, this work presents an efficient strategy to impart elastomers with outstanding energy dissipation properties, thereby opening up new avenues for the design of high-performance impact-protective and damping materials.

4. Materials and methods

Materials and methods are included in the ESI.†

Data availability

The data that support the findings of this study are available from the corresponding author upon reasonable request.

Author contributions

Fu-Long Gong: methodology, investigation, data curation, formal analysis, and writing – original draft. Shuang Long: data curation, investigation, methodology. Wenqing Lv: data curation, writing – review & editing. Xiaotong Shu: visualization, writing – review & editing. Bin Huang: investigation, writing – review & editing. Pingping Lou: investigation, writing – review & editing. Hua-Feng Fei: project administration, conceptualization, funding acquisition, resources, supervision, writing – review & editing. Zhijie Zhang: project administration, funding acquisition, resources, supervision.

Conflicts of interest

There are no conflicts to declare.

Acknowledgements

This research was supported by the National Key R&D Program of China (Grant No. 2024YFF0728500). The Analytical Instrumental Center for Physicochemical Analysis and Measurements, Chinese Academy of Sciences supported facilities used in this work.

References

1 Z. Yin, F. Hannard and F. Barthelat, *Science*, 2019, **364**, 1260–1263.
2 R. S. Lakes, T. Lee, A. Bersie and Y. C. Wang, *Nature*, 2001, **410**, 565–567.
3 F. Yuan, S. Wang, S. Zhang, Y. Wang, S. Xuan and X. Gong, *J. Mater. Chem. C*, 2019, **7**, 8412–8422.
4 L. Montero de Espinosa, W. Meesorn, D. Moatsou and C. Weder, *Chem. Rev.*, 2017, **117**, 12851–12892.
5 K. Liu, L. Cheng, N. Zhang, H. Pan, X. Fan, G. Li, Z. Zhang, D. Zhao, J. Zhao, X. Yang, Y. Wang, R. Bai, Y. Liu, Z. Liu, S. Wang, X. Gong, Z. Bao, G. Gu, W. Yu and X. Yan, *J. Am. Chem. Soc.*, 2021, **143**, 1162–1170.
6 J. Dong, Z.-H. Zhao and C.-H. Li, *Chem.–Eur. J.*, 2025, **31**, e202404397.
7 Z. Qin, Y. Yang, Q. Tian, H.-Y. Mi, H. Li, R. Guo, Y. Wang, C. Liu and C. Shen, *Chem. Eng. J.*, 2023, **467**, 143434.
8 H. Qiao, B. Wu, S. Sun and P. Wu, *J. Am. Chem. Soc.*, 2024, **146**, 7533–7542.
9 Z. Liu, S. J. Picken and N. A. M. Besseling, *Macromolecules*, 2014, **47**, 4531–4537.
10 W. Jiang, X. Gong, S. Wang, Q. Chen, H. Zhou, W. Jiang and S. Xuan, *Appl. Phys. Lett.*, 2014, **104**, 121915.
11 Y. Wang, L. Ding, C. Zhao, S. Wang, S. Xuan, H. Jiang and X. Gong, *Compos. Sci. Technol.*, 2018, **168**, 303–311.
12 M. Tang, W. Wang, D. Xu and Z. Wang, *Ind. Eng. Chem. Res.*, 2016, **55**, 12582–12589.
13 L. E. Porath and C. M. Evans, *Macromolecules*, 2021, **54**, 4782–4791.
14 A. Kurkin, Y. Lekina, D. G. Bradley, G. L. Seah, K. W. Tan, V. Lipik, J. V. Hanna, X. Zhang and A. l. Y. Tok, *Mater. Today Chem.*, 2023, **33**, 101677.
15 L. Porath, J. Huang, N. Ramlawi, M. Derkaloustian, R. H. Ewoldt and C. M. Evans, *Macromolecules*, 2022, **55**, 4450–4458.
16 J. Lee, B. B. Jing, L. E. Porath, N. R. Sottos and C. M. Evans, *Macromolecules*, 2020, **53**, 4741–4747.
17 C. Xu, Y. Wang, J. Wu, S. Song, S. Cao, S. Xuan, W. Jiang and X. Gong, *Compos. Sci. Technol.*, 2017, **153**, 168–177.
18 S. Zhang, S. Wang, Y. Wang, X. Fan, L. Ding, S. Xuan and X. Gong, *Composites, Part A*, 2018, **112**, 197–206.
19 S. Wang, S. Xuan, Y. Wang, C. Xu, Y. Mao, M. Liu, L. Bai, W. Jiang and X. Gong, *ACS Appl. Mater. Interfaces*, 2016, **8**, 4946–4954.
20 Z. Zhang, X. Lin, J. Lin, N. Liu, B. Wan, X. Fang, L. Shui, Y. Li, K. C. Tam, J. Huang and G. Zhou, *Chem. Eng. J.*, 2023, **473**, 145435.
21 C. S. Boland, U. Khan, G. Ryan, S. Barwich, R. Charifou, A. Harvey, C. Backes, Z. Li, M. S. Ferreira, M. E. Möbius, R. J. Young and J. N. Coleman, *Science*, 2016, **354**, 1257–1260.
22 T. Wu and B. Chen, *ACS Appl. Mater. Interfaces*, 2016, **8**, 24071–24078.
23 E. D'Elia, S. Barg, N. Ni, V. G. Rocha and E. Saiz, *Adv. Mater.*, 2015, **27**, 4788–4794.
24 Q. Wu, H. Xiong, Y. Peng, Y. Yang, J. Kang, G. Huang, X. Ren and J. Wu, *ACS Appl. Mater. Interfaces*, 2019, **11**, 19534–19540.
25 Y. Chen, X. Pu, M. Liu, S. Kuang, P. Zhang, Q. Hua, Z. Cong, W. Guo, W. Hu and Z. L. Wang, *ACS Nano*, 2019, **13**, 8936–8945.
26 Z. Chang, Y. He, H. Deng, X. Li, S. Wu, Y. Qiao, P. Wang and H. Zhou, *Adv. Funct. Mater.*, 2018, **28**, 1804777.
27 Z. Guo, L. Fan, C. Zhao, A. Chen, N. Liu, Y. Zhang and N. Zhang, *Adv. Mater.*, 2022, **34**, 2105133.
28 Y. Guo, C. Luo, M. Yang, H. Wang, W. Ma, K. Hu, L. Li, F. Wu and R. Chen, *Angew. Chem., Int. Ed.*, 2024, **63**, e202406597.
29 C. Huang, J. Zhou, S. Gu, P. Pan, Y. Hou, H. Xiong, T. Tang, Q. Wu and J. Wu, *ACS Appl. Mater. Interfaces*, 2023, **15**, 53242–53250.
30 D. Wang, C. Zhao, J. Yang, S. Lai, X. Wang and X. Gong, *Adv. Funct. Mater.*, 2024, **35**, 2419111.
31 Y. Yao, Z. Fan, M. Sang, X. Gong and S. Xuan, *Giant*, 2024, **18**, 100285.
32 N. Li, S. Gu, Q. Wu and J. Wu, *RSC Appl. Polym.*, 2025, **3**, 299–316.
33 W. Shi, T. Zhou, B. He, J. Huang and M. Liu, *Angew. Chem., Int. Ed.*, 2024, **63**, e202401845.
34 C. Zhao, X. Gong, S. Wang, W. Jiang and S. Xuan, *Cell Rep. Phys. Sci.*, 2020, **1**, 100266.
35 S. Ge, Y.-H. Tsao and C. M. Evans, *Nat. Commun.*, 2023, **14**, 7244.
36 J. Cheng, S. Fu, S. Ma, Z. Zhang, C. Ma and G. Zhang, *Adv. Mater.*, 2024, **36**, 2411700.
37 L. Cheng, J. Zhao, Z. Xiong, S. Liu, X. Yan and W. Yu, *Angew. Chem., Int. Ed.*, 2024, **63**, e202406937.
38 Q. Wu, Y. Peng, H. Xiong, Y. Hou, M. Cai, Y. Wang, L. Zhao and J. Wu, *Sci. China Mater.*, 2023, **66**, 4489–4498.
39 J. Cheng, Z. Zhang, K. Liu, C. Ma and G. Zhang, *Cell Rep. Phys. Sci.*, 2023, **4**, 101289.
40 A. Kurkin, V. Lipik, K. B. L. Tan, G. L. Seah, X. Zhang and A. I. Y. Tok, *Macromol. Mater. Eng.*, 2021, **306**, 2100360.
41 J. W. E. Weiss and D. L. Bryce, *J. Phys. Chem. A*, 2010, **114**, 5119–5131.
42 T. Yan, K. Schröter, F. Herbst, W. H. Binder and T. Thurn-Albrecht, *Macromolecules*, 2017, **50**, 2973–2985.
43 B. Soman and C. M. Evans, *Soft Matter*, 2021, **17**, 3569–3577.
44 J. Huang, Y. Xu, S. Qi, J. Zhou, W. Shi, T. Zhao and M. Liu, *Nat. Commun.*, 2021, **12**, 3610.
45 B. Liu, C. Du, H. Deng, Y. Fu, F. Guo, L. Song and X. Gong, *Polymer*, 2022, **247**, 124800.

46 Q. Li, W. Li, Z. Liu, S. Zheng, X. Wang, J. Xiong and F. Yan, *Adv. Mater.*, 2024, **36**, 2311214.
47 M. Tang, P. Zheng, K. Wang, Y. Qin, Y. Jiang, Y. Cheng, Z. Li and L. Wu, *J. Mater. Chem. A*, 2019, **7**, 27278–27288.
48 C. Chen, H.-F. Fei, J. J. Watkins and A. J. Crosby, *J. Mater. Chem. A*, 2022, **10**, 11667–11675.
49 R. Guo, Q. Zhang, Y. Wu, H. Chen, Y. Liu, J. Wang, X. Duan, Q. Chen, Z. Ge and Y. Zhang, *Adv. Mater.*, 2023, **35**, 2212130.
50 J. Zhou, Q. Wu, P. Pan, H. Xiong, Y. Hou, Y. Chen, J. Wu and T. Tang, *ACS Appl. Bio Mater.*, 2024, **7**, 1694–1702.
51 P. Qu, C. Lv, Y. Qi, L. Bai and J. Zheng, *ACS Appl. Mater. Interfaces*, 2021, **13**, 9043–9052.
52 Z. Lin, C. Chen, H. Huang, B. Xu, Y. Zhuang and R.-J. Xie, *Sci. China Mater.*, 2023, **66**, 4464–4472.
53 S. Rao, X. Zeng, X. Cheng, J. Fan, D. He, L. Ren, G. Du and X. Zeng, *Chem. Eng. J.*, 2023, **474**, 145847.
54 R. H. Ewoldt, P. Winter, J. Maxey and G. H. McKinley, *Rheol. Acta*, 2010, **49**, 191–212.
55 H. Xiang, X. Li, B. Wu, S. Sun and P. Wu, *Adv. Mater.*, 2023, **35**, 2209581.
56 Z. Xu, M. Wu, W. Gao and H. Bai, *Sci. Adv.*, 2022, **8**, eabo0946.
57 H. Chen, M. Sang, Y. Pan, S. Duan, Y. Hu and X. Gong, *ACS Appl. Mater. Interfaces*, 2024, **16**, 62639–62653.
58 J. Cheng, X. Yao, Z. Zhang, Y. Tan, N. Hu, C. Ma and G. Zhang, *Mater. Horiz.*, 2024, **11**, 3143–3156.